Multi-stage creep behavior of frozen granular soils: Experimental evidence and constitutive modeling

Ulrich Schindler[1,*], Roberto Cudmani[1,2,+], Stylianos Chrisopoulos[1,3,+], and Andreas Schünemann[1,4]

[1]Technical University of Munich, Department of Civil, Geo and Environmental Engineering, Chair of Soil Mechanics and Foundation Engineering, Rock Mechanics and Tunnelling, Franz-Langinger-Str. 10, 81245 Munich, Germany

[*] u.schindler@tum.de, corresponding author

[2] r.cudmani@tum.de

[3] s.chrisopoulos@tum.de

[4] a.schuenemann@tum.de

[+] R. Cudmani and S. Chrisopoulos have contributed equally to this work.

Abstract

The significance of ground freezing is becoming ever more germane as the design of new urban tunneling systems requires more complex geometries and higher bearing capacities, which are limited with conventional construction methods. Ground freezing is an advanced construction technique to make the water-saturated subsoil impermeable and temporarily increase its strength and stiffness. This study reports experimental investigations consisting of single-stage and multi-stage creep tests under uniaxial loading. The comparison of the different loading types reveals the influence of the stress-strain history on the rate- and temperature-dependent behavior of frozen granular soils. We extend the constitutive model for frozen soils proposed by Cudmani et al. (2022) to consider stepwise loading and creep by coupling creep time with stress-strain history. Moreover, we simulate element tests and compare the simulations with our own experimental data as well as data from the literature to achieve the first step in validating the extended model. The good agreement of the numerical and experimental results confirms the constitutive model's ability to capture the main features of the complex mechanical behavior of frozen granular soils for single-stage as well as multi-stage loading under constant temperatures.

Keywords: ground freezing, frozen soil, creep, constitutive model, element tests

1 Introduction

Ground freezing is widely used in geotechnical applications to temporarily increase the strength and stiffness of the subsoil and provide water tightness below the groundwater table. Ground freezing has many advantages over other ground stabilization techniques. On the one hand, it has a relatively low environmental impact. On the other hand, owing to its versatility and reliable quality control through temperature measurements, ground freezing is often preferable to other available soil improvement techniques in urban situations with complex boundary conditions (Harris, 1995; Andersland and Ladanyi, 2003). Many ground freezing applications can be found in the literature, e.g., for the construction of underground stations, excavation of cross passages to connect tunnel tubes and building underpinning (e.g., (Cudmani and Nagelsdiek, 2006; Russo et al., 2015; Han et al., 2016; Orth, 2018; Pimentel and Anagnostou, 2019)). Recently, the intensive use of ground freezing to excavate the cross passages under the Suez Canal (Egypt) impressively demonstrated the importance of ground freezing in modern tunnel constructions (Phillips et al., 2021).

In general, frozen soil bodies supporting tunnel excavations exhibit varying stress states and different loading types through the construction stages (Andersland and Ladanyi, 2003; Orth, 2018). The excavation leads to the shearing of the frozen soil and a relatively rapid increase in stress. After completing the excavation, the frozen soil body deforms under a predominantly constant stress state and must support the soil above it until the completion of the tunnel lining. Common excavation techniques, such as partial face advance, result in a stepwise increased loading of the frozen soil body. Russo et al. (2015) reported three long-duration excavation steps during the challenging construction of the Toledo underground station in Naples (Italy). Several excavation stages with different lengths of advance induced a stepwise increased loading on the supporting frozen soil over a period of more than six months. Classen et al. (2019) and Zhou et al. (2021) considered the application of ground freezing to support very large tunnel excavations with up to fourteen excavation stages. From a practical point of view, these and other examples clearly highlight the need to improve our fundamental understanding of the influence of the loading history on the mechanical behavior of frozen granular soils.
Eckardt (1979b,a, 1982) extensively investigated the creep behavior of frozen medium sand samples under uniaxial loading conditions. Single-stage and multi-stage creep tests were carried out. In the single-stage creep test, the load was increased monotonically to the desired value and then maintained constant. In the multi-stage creep tests, Eckardt (1979b,a, 1982) applied the same final load as in the single-stage creep tests, but this was achieved stepwise. In each loading step, creep was allowed during a period before the next load increment was applied. In single-stage as well as multi-stage creep tests, Eckardt observed primary (decreasing creep rates), secondary (nearly constant creep rates), and tertiary creep (increasing creep rates) according to the definitions proposed by Orth (1986) and Andersland and Ladanyi (2003). Moreover, the different strain evolutions resulting from the single-stage and multi-stage creep tests evidenced the influence of the stress and strain history on the creep behavior. Indeed, Eckardt (1979b,a, 1982) also concluded that during secondary creep, the strain evolution of both test types is similar and thus independent of the stress-strain history. Nevertheless, the evaluation of creep strain rates for different stress histories supporting this conclusion is missing in this study. Therefore, the

equivalence of single-stage and multi-stage loading regarding the creep behavior of frozen soils has not been conclusively clarified. Indeed, numerous studies like (Andersland and Akili, 1967; Vyalov et al., 1989; Zhou et al., 2020) have contributed to the understanding of the complex mechanical behavior of frozen soils depending on the stress and strain history. However, the influence of the stress and strain history on the rate-, stress-, and temperature-dependent mechanical behavior of frozen soils is not yet fully understood.

According to Zhao et al. (2023) and Cudmani et al. (2022), there are many constitutive models to either predict the shear or the creep behavior of frozen soils. Nevertheless, there is a lack of sophisticated models able to capture the rate-, stress-, and temperature-dependent behavior of frozen soils under compressive and tensile loading. In addition, only a few models in the literature take into account the influence of the confining pressure on the shear resistance and creep behavior of frozen soils. The model proposed by Cudmani et al. (2022) intends to fill this gap and is already validated for predominantly monotonic loading. However, the consideration of stress-strain histories deviating from monotonic loading (e.g., stepwise, loading-unloading) on the mechanical behavior of frozen soils is still missing. In fact, there are many novel constitutive models for frozen soils (e.g., (Ghoreishian Amiri et al., 2016; Xu et al., 2017; Yao et al., 2018)), which neither take into account nor are validated for stepwise loading.

This study aims to present an important and impactful contribution to the following ends: First, we introduce a comprehensive experimental program including uniaxial single-stage and multi-stage creep tests to observe, understand, and quantify the main characteristics of the stress-strain history on the mechanical behavior of frozen granular soils. Here, the objective is to extend the existing constitutive model by Cudmani et al. (2022) to consider stepwise loading and creep based on our experimental findings. Subsequently, the focus is placed on the model validation for multi-stage creep using element tests. Here, we compare our numerical results with our own experiments as well as data from the literature.

2 Uniaxial single- and multi-stage creep tests

2.1 Testing material, sample preparation, and testing program

Table 1 includes the physical properties, and Figure 1 the grain size distribution curve of the tested frozen sand.

Table 1: Physical properties of the tested frozen sand

e_{min} / e_{max} [-]	$d_{10}/d_{30}/d_{60}$ [mm]	ρ_s [g/cm^3]
0.52/0.82	0.44/0.53/0.64	2.65

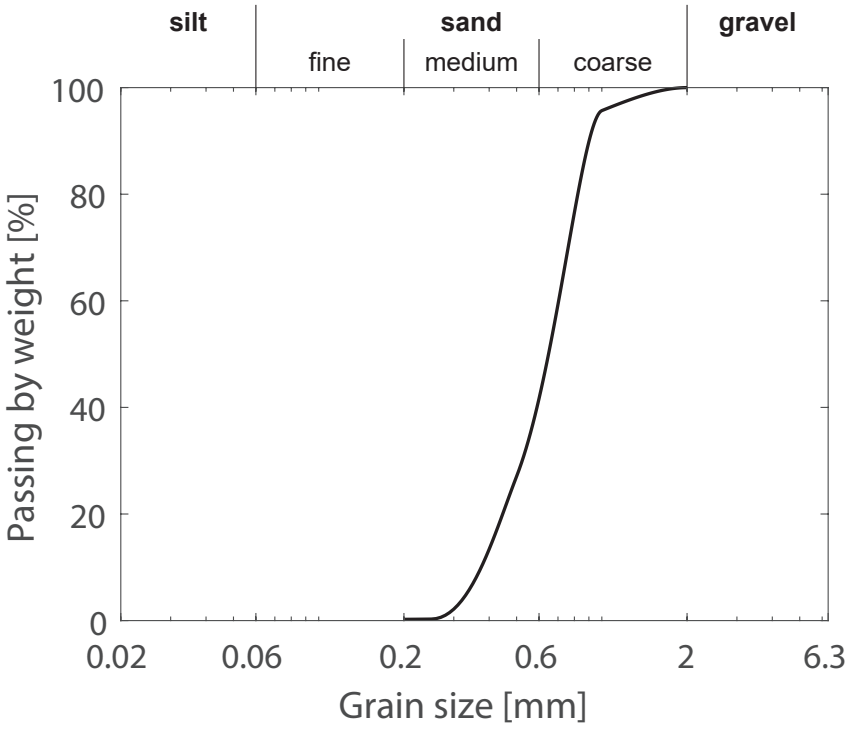

Figure 1: Grain size distribution of the tested frozen sand

The tested samples were circular and had a diameter of about 50 mm and a height of about 100 mm. They were prepared with the water-sedimentation method (see (Lade, 2016) for further details). Afterward, the samples were additionally compacted on a vibrating table. Subsequently, the specimens were frozen isotropically in a freezer to a temperature of $\theta = -4.3$ °C. The preparation method led to a dense state with an average dry density of $\rho_\mathrm{d} = 1.66\mathrm{g/cm}^3$ and a water content of w = 0.20. We cut a few samples into several parts and determined their grain size distribution, water content, and dry density. The results for each part were similar, thus confirming the soil sample homogeneity and reproducibility using the selected preparation method. Nevertheless, according to Lade (2016), it is difficult to achieve a full saturation of the soil samples by using the water-sedimentation method. In this study, the specimens were not fully saturated and had an average saturation degree of $\mathrm{S_r} \approx 90$ %. In fact, studies like (Enokido and Kameta, 1987)

indicate that saturation degrees below 80-85% strongly affect the essential mechanical behavior of frozen coarse-grained soils. In contrast, the influence of partial saturation with $S_r \geq 90$ % on the shear and creep behavior of frozen sand is relatively small, and its mechanical behavior is comparable to fully saturated conditions.
Before testing and in accordance with Orth (1986), the sample end plates were trimmed and smoothed out. Moreover, silicone grease on a Teflon layer was used as lubrication between the specimen and the load frame to reduce friction. In addition, the samples were wrapped in a rubber cover to prevent sublimation during the tests.

In order to investigate the influence of the loading history on the creep behavior, a series of uniaxial single-stage and multi-stage creep tests on frozen sand were performed at Zentrum Geotechnik of the Technical University of Munich. The tests were conducted in a climatic chamber (air temperature cooling of the specimens) using a dead load oedometer test apparatus. Hence, the loading speed during the tests was relatively fast as the weight discs for the load application were applied manually and instantaneously after each other. Moreover, the load application occurred after the samples were frozen, resulting in post-freezing confinement, as described by Nishimura and Wang (2019). Figure 2 illustrates the testing procedure for the two different load types. In the single-stage creep test, vertical pressure was monotonically applied, and then the stress was kept constant as the frozen soil samples crept. In contrast, the multi-stage creep test consisted of three loading stages. After the initial loading stage, the second and third load increases occurred after an axial strain $\epsilon_1 = 2.5$ % and $\epsilon_1 = 3.5$ %, respectively. In each step, the load was maintained constant, and the creep deformations of the frozen soil samples were monitored.

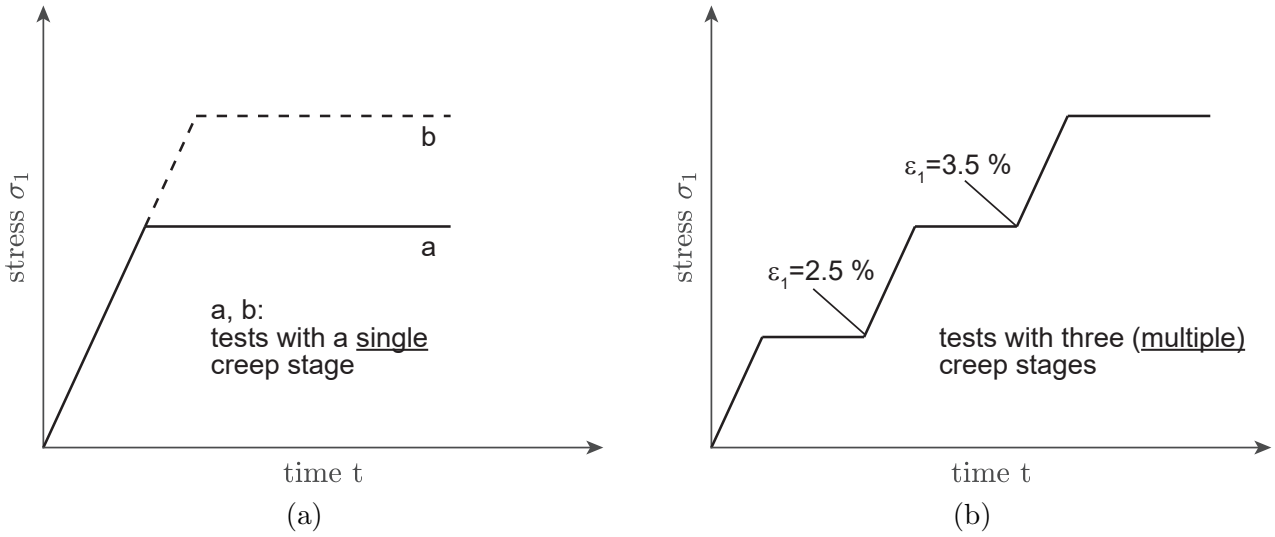

Figure 2: Test procedure for a) single-stage creep tests; b) multi-stage creep tests

The testing program, including six single-stage and three multi-stage creep tests, is summarized in Table 2.

Table 2: Uniaxial creep tests on frozen sand at $\theta = -4.3$ °C

Test number	σ_1 [kN/m^2]
Single-stage tests	
ST1	2.5
ST2	3.0
ST3	3.5
ST4	4.0
ST5	4.5
ST6	5.0
Multi-stage tests	
MT1	2.5/3.0/3.5
MT2	3.0/3.5/4.0
MT3	4.0/4.5/5.0

2.2 Test results

The results of the single-stage and multi-stage creep tests are compared in Figure 3 and include the plotted total strain evolution (left side) and the total strain rate evolution (right side) over the testing time. However, for the creep stage, the plotted total strains in Figure 3 are predominantly viscoplastic. The single creep tests (symbols) in Figure 3 show the well-known creep behavior of frozen soils (e.g., (Andersland and Ladanyi, 2003)): On the one hand, the axial strain increases with time. On the other hand, the strain rate first decreases (primary creep) and then increases (tertiary creep) with time. The testing time, at which the minimum axial strain rate $\dot{\epsilon}_\mathrm{m}$ (secondary creep) is reached, and the tertiary creep begins, is called lifetime $\mathrm{t_m}$, according to Orth (1986) and Cudmani et al. (2022).

In principle, the multi-stage creep tests (solid and dashed lines) in Figure 3a)-c) reveal a similar evolution of axial strain over time as the single-stage creep tests. However, the strain evolution resulting from the multi-stage creep tests lies between that of the single-stage tests. As seen on the right side of Figure 3, the load increase in the multi-stage creep tests led to a jump in the strain rate. As expected, during the first loading stage, the evolution of the axial strain rate is similar in both the multi-stage and the corresponding single-stage creep tests. At the beginning of the second and third creep stage, the strain rate in the multi-stage creep tests lies above that of the corresponding single-stage creep tests for the same testing time. With increasing time, the strain rate approaches that of the single-stage creep tests. Deviations from this behavior pattern occur when the third and last creep stage begins near the lifetime $\mathrm{t_m}$ (the turning point of the strain evolution), as can be seen in test MT3 in Figure 3c). In this case, the axial strain rate does not decrease anymore with time. Instead, it remains almost constant over a relatively short period of time and then increases, thus indicating the beginning of tertiary creep. Here, the behavior of the frozen soil becomes unstable. We note that both the deviatoric stress level and the previous stress history influence the lifetime $\mathrm{t_m}$, while the minimum axial strain rate $\dot{\epsilon}_\mathrm{m}$ at the turning point depends only on the deviatoric stress level.

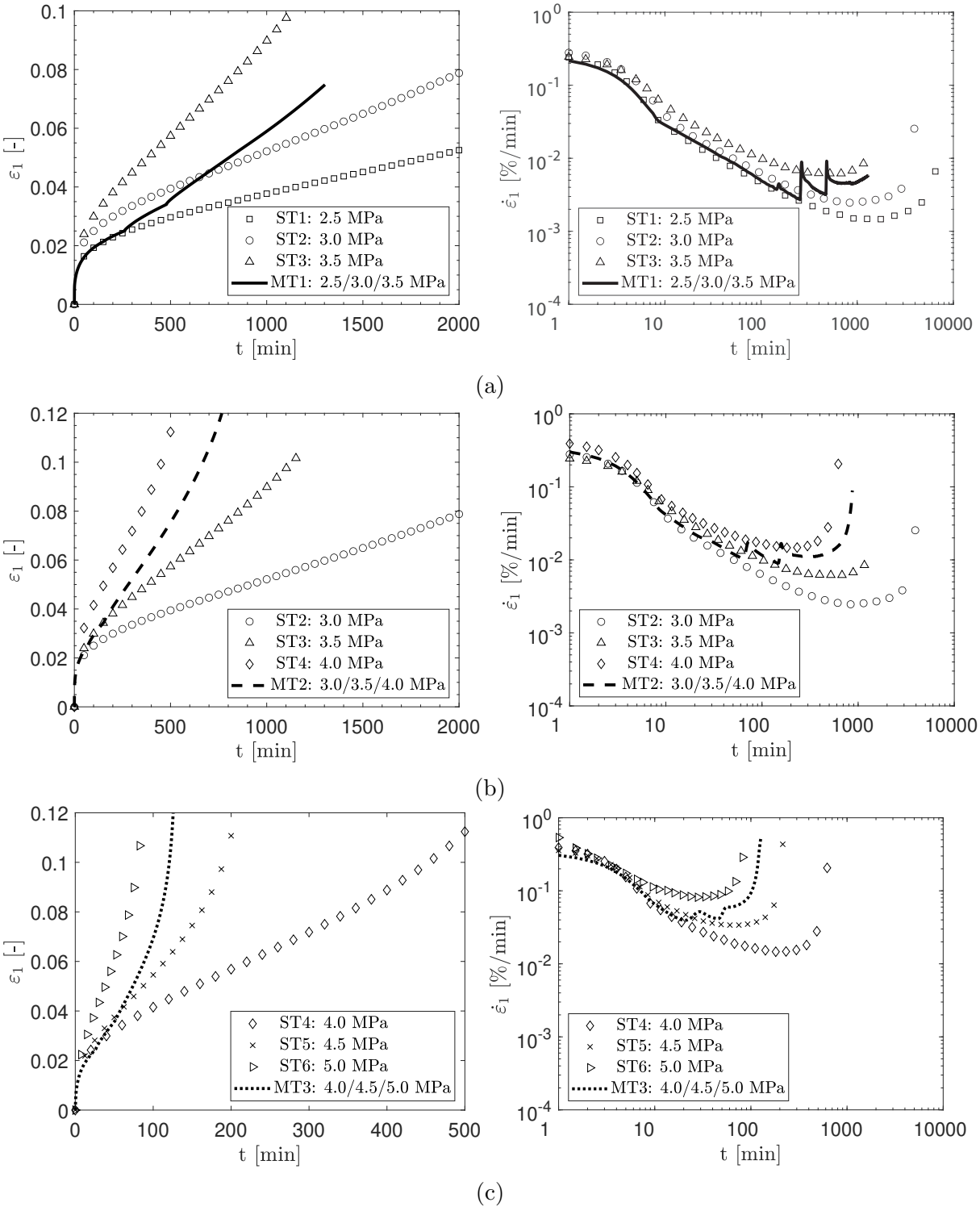

Figure 3: Results of the single- (symbols) and multi-stage (lines) creep tests at $\theta = -4.3$ °C: left: evolution of axial strain over time; right: evolution of axial strain rate over time

Based on the results of uniaxial single-stage creep tests, Ting et al. (1983) and Orth (1986) concluded that the total axial strain at the turning point is roughly independent of the temperature θ and the axial stress σ_1. Figure 4 shows the average axial strain ϵ_m at the turning point ($t = t_m$) for our tests compared with test results published by Orth (1986), which were obtained using frozen sand similar to that described in Section 2.1.

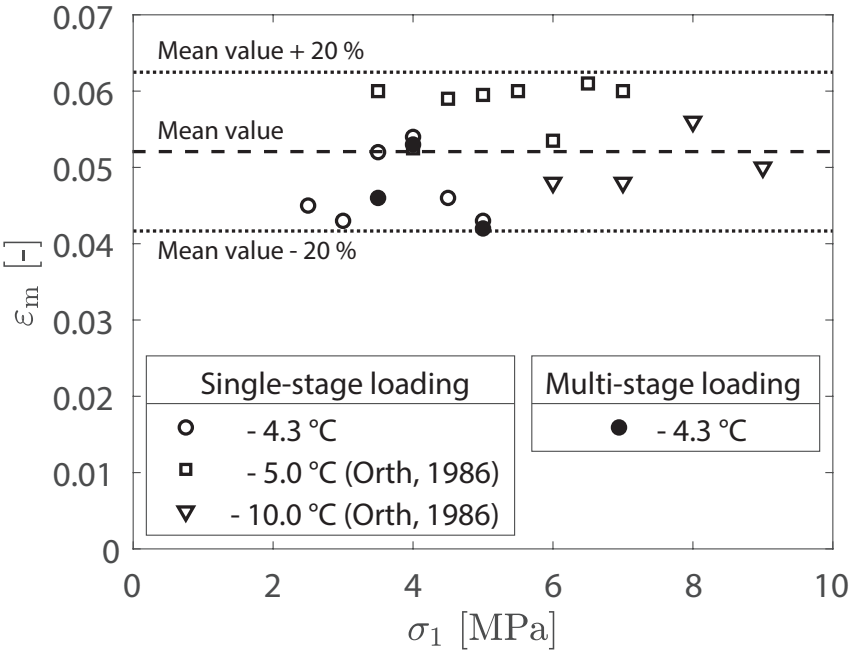

Figure 4: Average axial strain ϵ_m at the turning point ($t = t_m$) for uniaxial single-stage and multi-stage creep tests for different stresses and temperatures

According to Orth (1986), the observed scatter of ϵ_m in Figure 4 can be traced back to differences when setting up the sample end plates before the start of the tests. In addition, slight differences in the initial density and degree of saturation of the samples could also contribute to this scattering. As can be seen, the results of our single-stage and multi-stage creep tests confirm the findings of Ting et al. (1983) and Orth (1986) regarding the negligible influence of the temperature θ and the axial stress σ_1 on ϵ_m. In addition, since the total average axial strains ϵ_m determined in the single-stage and multi-stage tests are in the same range (see Figure 4), the independence of ϵ_m from the loading history can also be assumed. Nevertheless, further investigations with more general loading and creep stages are required to validate this preliminary assumption fully.

3 Conceptual framework to consider the influence of the loading history on the creep behavior of frozen soils

A crucial relationship of the constitutive model for frozen granular soils proposed by Cudmani et al. (2022) is the relationship between the normalized axial strain rate $\dot{\epsilon}_1/\dot{\epsilon}_m$ and the normalized time t/t_m. According to Orth (1986) and Cudmani et al. (2022), for single-stage creep and monotonic shearing with constant strain rate, this relationship is independent of the temperature and the stress level and can be described by Equation 1.

$$\frac{\dot{\epsilon}_1}{\dot{\epsilon}_m} = \exp(\beta) \exp\left(\beta \frac{t}{t_m}\right) \left(\frac{t}{t_m}\right)^{-\beta} \tag{1}$$

Here, $\dot{\epsilon}_m$ is the minimum axial strain rate, t_m is the lifetime, and β is a material parameter. As shown by the experimental results of the multi-stage creep tests in Section 2.2, in contrast to $\dot{\epsilon}_m$, the lifetime t_m depends on the loading history. For this reason, Equation 1, which establishes a unique relationship between t_m and $\dot{\epsilon}_m$, is unable to describe the creep behavior observed in the multi-stage creep tests.
In the following, a time transformation procedure is proposed to capture the behavior observed in the multi-stage creep tests using Equation 1. The proposed procedure is based on the following assumptions derived from the experimental results discussed in Section 2.2. Assumptions a)-f):

a) All tested frozen soil specimens had the same initial density, degree of saturation, and amount of frozen pore water.

b) The total stress is equal to the creep stress.

c) The average axial strain ϵ_m at the turning point is mostly independent of the temperature, axial stress, and loading history, as shown by the experimental results in Figure 4. Thus, ϵ_m can be considered as a material parameter.

d) The minimum axial strain rate $\dot{\epsilon}_m$ depends only on the temperature and the axial stress. A possible dependence of $\dot{\epsilon}_m$ on the loading history can be disregarded, as indicated by the experimental results in Figure 3.

e) The lifetime t_m depends on the temperature, the axial stress, and the loading history.

f) There is a unique relationship between the strain rate $\dot{\epsilon}_1$, the strain ϵ_1, and the stress σ_1. This relationship does not depend on the loading history.

Figure 5 illustrates the developed procedure to transform the creep time t and the "lifetime" t_m determined in multi-stage creep tests into an equivalent time and lifetime of the corresponding single-stage creep tests.

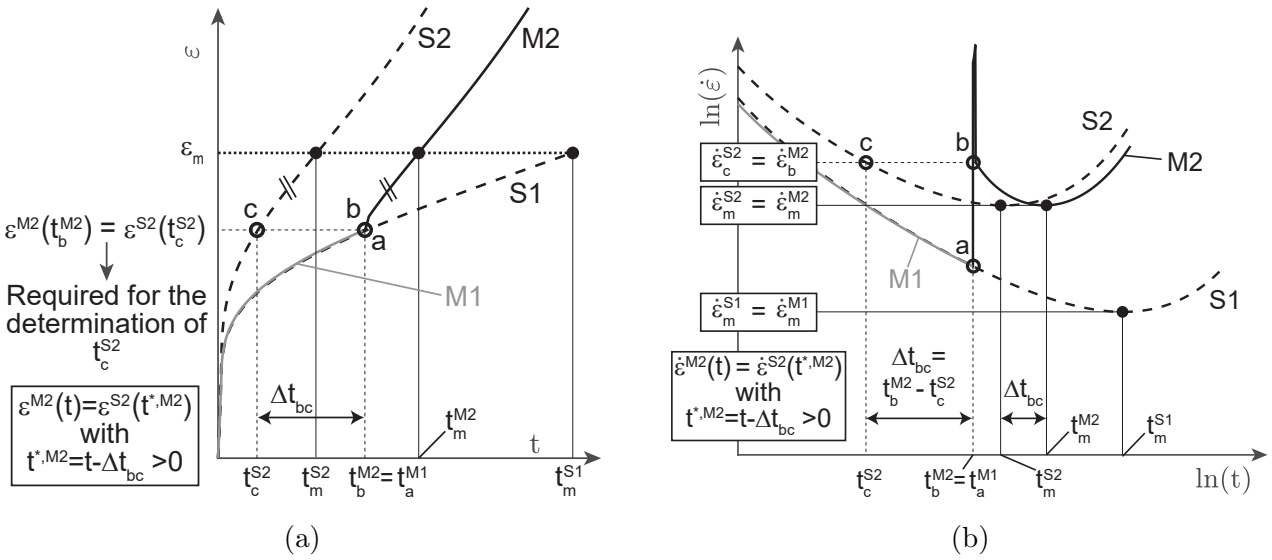

Figure 5: Determination of the normalized axial strain rate $\dot{\epsilon}_1/\dot{\epsilon}_m$ over normalized time t/t_m for a multi-stage creep test M consisting of the loading stages M1 and M2 compared to the single-stage creep tests S1 and S2 with $\sigma^{S1} = \sigma^{M1}$ and $\sigma^{S2} = \sigma^{M2}$ under a constant temperature

The sub-index S denotes single-stage and M multi-stage creep tests for the same temperature. For simplicity, the multi-stage creep test M assumably consists of two loading stages, M1 and M2. The stepwise-applied stresses σ^{M1} and σ^{M2} are equal to those in the single-stage creep tests S1 and S2, with $\sigma^{S1} = \sigma^{M1}$ and $\sigma^{S2} = \sigma^{M2}$. In addition, t describes the actual testing time. Naturally, the time t, the strain ϵ, and the strain rate $\dot{\epsilon}_m$ of test M1 are identical to test S1 during the first loading stage. Hence, the actual strain rate $\dot{\epsilon}^{S1} = \dot{\epsilon}^{M1}$, the corresponding minimum strain rate $\dot{\epsilon}_m^{S1} = \dot{\epsilon}_m^{M1}$, and lifetime $t_m^{M1} = t_m^{S1}$ are also the same. As can be seen in Figure 5b, it is assumed that the frozen soil sample has not achieved the lifetime during stage M1.

At the end of the first loading stage, M1 at $t = t_a^{M1} = t_b^{M2}$, the stress increases from σ^{M1} to σ^{M2} (see Figure 5a). In accordance with the aforementioned assumptions c)-f), the relationship $\epsilon^{M2}(t) = \epsilon^{S2}(t)$ must be fulfilled for $t \geq t_b^{M2}$ and $t \geq t_c^{S2}$, respectively. Thus as shown in Figure 5a, the strain versus time curves for M2 and S2 are identical starting from points b and c, but they are shifted by a period of time $\Delta t_{bc} = t_b^{M2} - t_c^{S2}$. Using the condition $\epsilon^{M2}\left(t_b^{M2}\right) = \epsilon^{S2}\left(t_c^{S2}\right)$ and assuming that $\epsilon^{S2}\left(t_c^{S2}\right)$ is known from the single-stage test, the value of t_c^{S2} can be determined to calculate the time shift Δt_{bc}. According to Figure 5a, the transformed time $t^{*,M2} = t - \Delta t_{bc}$ in combination with $\epsilon^{M2}(t) = \epsilon^{S2}\left(t^{*,M2}\right)$ for $t^{*,M2} > 0$ describes the creep behavior in the loading stage M2 based on the corresponding single-stage creep test. The transformed lifetime for M2 is $t_m^{*M2} = t_m^{S2} = t_m^{M2} - \Delta t_{bc}$ derived from the lifetime t_m^{S2} of the single-stage test S2.

Summarizing, the transformed time $t^{*,M2}$ is the time in a single-stage creep test required to achieve the deformation $\epsilon^{M2}\left(t > t_b^{M2}\right)$ with $\sigma^{S2} = \sigma^{M2}$. In particular, $t^{*,M2}$ at the point b of M2 equals $t_b^{*,M2} = t_b^{M2} - \left(t_b^{M2} - t_c^{S2}\right) = t_c^{S2}$. According to the assumption c), both samples M2 and S2 achieve the same strain $\epsilon_m = \epsilon^{M2}\left(t_m^{M2}\right) = \epsilon^{S2}\left(t_m^{S2}\right)$ and the same minimum strain rate $\dot{\epsilon}^{M2}\left(t_m^{M2}\right) = \dot{\epsilon}^{S2}\left(t_m^{S2}\right)$ at the turning point. In accordance with the

above-described time transformation procedure, we propose the following equations to calculate the time-dependent evolution of the strain rate $\dot{\epsilon}^{M2}(t)$ for the loading stage M2 based on the results of the corresponding single-stage creep test S2:

$$\frac{\dot{\epsilon}^{S2}\left(t^{*,M2}\right)}{\dot{\epsilon}_m^{S2}} = \exp(\beta)\exp\left(\beta\frac{t^{*,M2}}{t_m^{*,M2}}\right)\left(\frac{t^{*,M2}}{t_m^{*,M2}}\right)^{-\beta} \tag{2}$$

$$t^{*,M2} = t - \Delta t_{bc} \text{ with } t > 0 \text{ and } t > \Delta t_{bc} \tag{3}$$

$$t_m^{*M2} = t_m^{M2} - \Delta t_{bc} = t_m^{S2} \tag{4}$$

$$\dot{\epsilon}^{M2}(t) = \dot{\epsilon}^{S2}\left(t^{*,M2}\right) \tag{5}$$

In addition, the equations 2-5 can be generalized to describe the strain rate in the loading stage Mj of a multi-stage creep test consisting of n stages based on their corresponding single-stage test Sj. The loading stage number is defined with the superscript index j and the corresponding time increment with the subscript index i:

$$\frac{\dot{\epsilon}^{Sj}\left(t^{*,Mj}\right)}{\dot{\epsilon}_m^{Sj}} = \exp(\beta)\exp\left(\beta\frac{t^{*,Mj}}{t_m^{*,Mj}}\right)\left(\frac{t^{*,Mj}}{t_m^{*,Mj}}\right)^{-\beta} \tag{6}$$

$$t^{*,Mj} = t - \Delta t_i \text{ with } t > 0 \text{ and } t > \Delta t_i \tag{7}$$

$$t_m^{*Mj} = t_m^{Sj} \tag{8}$$

$$\dot{\epsilon}^{Mj}(t) = \dot{\epsilon}^{Sj}\left(t^{*,Mj}\right) \tag{9}$$

Here, $\Delta t_i = t_0^{Mj} - t_0^{Sj}$ is the time difference between the beginning of M^j at t_0^{Mj} and the single-stage creep time t_0^{Sj}, at which $\epsilon^{Mj}\left(t_0^{Mj}\right)$ equals $\epsilon^{Sj}\left(t_0^{Sj}\right)$. In addition, the multi-stage and single-stage creep behavior for the loading stage $j = 1$ and time increment $i = 1$ correspond to $t = t_0^{S1} = t_0^{M1}$, $\Delta t_1 = 0$ and $t^{*,M1} = t^{S1} = t$.

To sum up, Figure 6 compares both the normalized axial strain rate $\dot{\epsilon}_1/\dot{\epsilon}_m$ over normalized time t/t_m for the single-stage creep tests presented in Figure 3, as well as $\dot{\epsilon}_1/\dot{\epsilon}_m$ over the normalized transformed time $t^{*,Mj}/t_m^{*,Mj}$ for the additional multi-stage creep tests. In accordance with the proposed time transformation procedure, the multi-stage test results are converted to equivalent single-stage tests, and therefore, as expected, both single- and multi-stage test results converge to Equation 1.

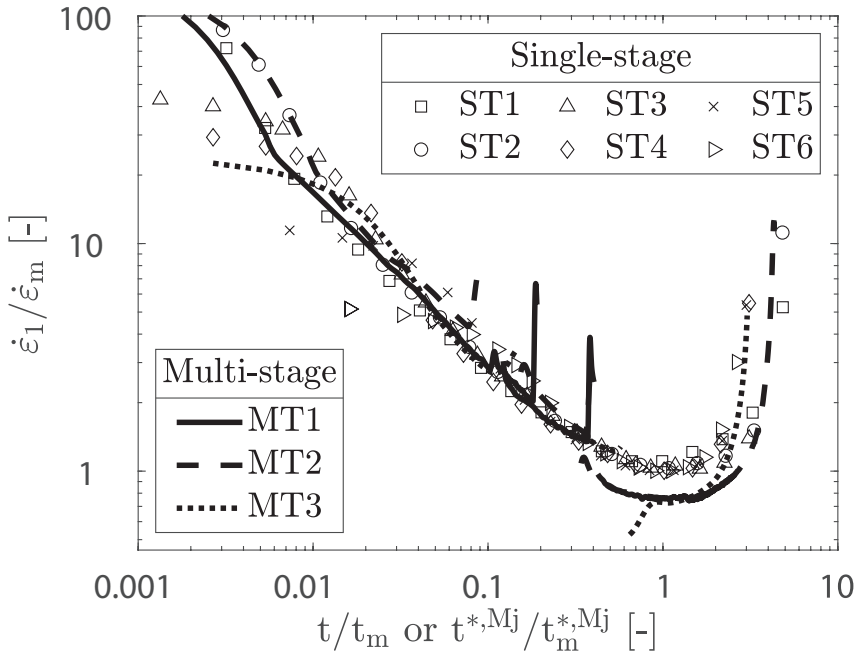

Figure 6: Uniaxial creep tests at $\theta = -4.3$ °C according to Table 2: Evolution of the normalized axial strain rate $\dot{\epsilon}_1/\dot{\epsilon}_m$ over normalized time t/t_m for the single-stage as well as $\dot{\epsilon}_1/\dot{\epsilon}_m$ over the normalized transformed time $t^{*,Mj}/t_m^{*,Mj}$ for the multi-stage creep tests

In summary, the evolution of the axial strain rate for multi-stage creep depends on the temperature, the axial stress, and the loading history. The latter influence only the lifetime t_m but not the minimum axial strain rate $\dot{\epsilon}_m$. In the following, the existing constitutive model for frozen granular soils proposed by Cudmani et al. (2022) will be extended to take into account the influence of the previous loading history on the stress-strain behavior based on the conceptual model presented in this section.

4 Extension of the constitutive model to consider multi-stage creep

4.1 Constitutive model for predominantly monotonic loading, according to Cudmani et al. (2022)

Cudmani et al. (2022) developed a constitutive model for predominantly monotonic loading that takes into account the influence of the confining pressure and differentiates between compressive and tensile strength and creep. In this section, only the basic equations of the model are presented; for further details, see Cudmani et al. (2022). The elastic-viscoplastic model for frozen granular soils is based on a rheological model of the Maxwell type ($\dot{\boldsymbol{\epsilon}} = \dot{\boldsymbol{\epsilon}}_\mathrm{e} + \dot{\boldsymbol{\epsilon}}_\mathrm{v}$)):

$$\dot{\boldsymbol{\sigma}} = \mathbf{L} : (\dot{\boldsymbol{\epsilon}} - \dot{\boldsymbol{\epsilon}}_\mathrm{v}) \tag{10}$$

where $\dot{\boldsymbol{\sigma}}$ is the stress rate tensor, $\dot{\boldsymbol{\epsilon}}$ is the total strain rate tensor, $\dot{\boldsymbol{\epsilon}}_\mathrm{v}$ is the viscous strain rate tensor, and $\mathbf{L}$ is the fourth-order isotropic elastic stiffness tensor. The isotropic elastic stiffness tensor can be expressed in terms of Young's modulus E and Poisson's ratio ν, see details in (Cudmani et al., 2022).
The viscous strain rate tensor for a general stress state can be obtained from the following equation:

$$\dot{\boldsymbol{\epsilon}}_\mathrm{v} = ||\dot{\boldsymbol{\epsilon}}_\mathrm{m}||\, \exp(-\beta) \exp\left(\beta \frac{\mathrm{t}}{\mathrm{t_m}}\right) \left(\frac{\mathrm{t}}{\mathrm{t_m}}\right)^{-\beta} \frac{\mathbf{s}}{||\mathbf{s}||} \tag{11}$$

where $\mathbf{s}$ is the deviatoric stress tensor, and β is a dimensionsless material constant. The minimum creep rate $||\dot{\boldsymbol{\epsilon}}_\mathrm{m}||$ can be obtained by Equation 12.

$$||\dot{\boldsymbol{\epsilon}}_\mathrm{m}|| = \sqrt{\frac{3}{2}}\, \dot{\epsilon}_\alpha\, \exp\left[\left(\frac{\mathrm{K_1}}{\theta + 273.4} + \ln \dot{\epsilon}_\alpha\right)\left(\frac{\sigma_\mathrm{cr}(\mathrm{p,q},\phi)}{\sigma_\alpha(\theta)} - 1\right)\right] \tag{12}$$

Here, θ represents the temperature in Celcius, $\mathrm{K_1}$ is a material constant, $\dot{\epsilon}_\alpha$ is a reference strain rate ($\dot{\epsilon}_\alpha = 1\%/\mathrm{min}$), while the temperature-dependent uniaxial reference stress σ_α at the reference strain rate, the lifetime $\mathrm{t_m}$, and the equivalent uniaxial creep strength σ_cr are defined in Equations 13-15, respectively.

$$\sigma_\alpha(\theta) = \alpha_1(-\theta)^{\alpha_2} \tag{13}$$

$$\mathrm{t_m} = \sqrt{\frac{3}{2}}\, \mathrm{c}/||\dot{\boldsymbol{\epsilon}}_\mathrm{m}|| \tag{14}$$

$$\sigma_\mathrm{cr}(\mathrm{p,q},\phi) = \tfrac{1}{2}\left\{\left[\left(\mathrm{B}\cos\left(\phi - \tfrac{\pi}{3}\right) + \mathrm{C}\right)\mathrm{q} + \mathrm{Dp}\right] + \sqrt{\left[\left(\mathrm{B}\cos\left(\phi - \tfrac{\pi}{3}\right) + \mathrm{C}\right)\mathrm{q} + \mathrm{Dp}\right]^2 + 4\mathrm{Aq}^2}\right\} \tag{15}$$

The parameters α_1, α_2, and c in Equations 13 and 14 are material constants of the 1D model. In Equation 15 the parameters A, B, C, and D represent material constants of the 3D model, while p and q denote the Roscoe stress invariants, and ϕ denotes Lode angle. In this paper, the mechanical sign convention is used, i.e., compressive stress is negative and tensile stress positive. Therefore, the Lode angle for compressive stress is $\phi = \frac{\pi}{3}$ and for tensile stress, it is $\phi = 0$.

4.2 Generalization of the transformed creep time

The constitutive model developed by Cudmani et al. (2022) simulates the time-dependent stress-strain behavior of frozen soils for predominantly monotonic loading. As described in Section 3, the behavior observed in a multi-stage creep test can also be predicted with Equation 1, originally valid for single-stage creep tests, with the help of a time transformation. In this section, this concept is generalized to consider the influence of multi-stage stress paths on the mechanical behavior of frozen soils.

Figure 7 illustrates the proposed extension of the constitutive model to consider multi-stage creep. Here, the loading stage number is defined with the superscript index j and the corresponding time increment with the subscript index i.

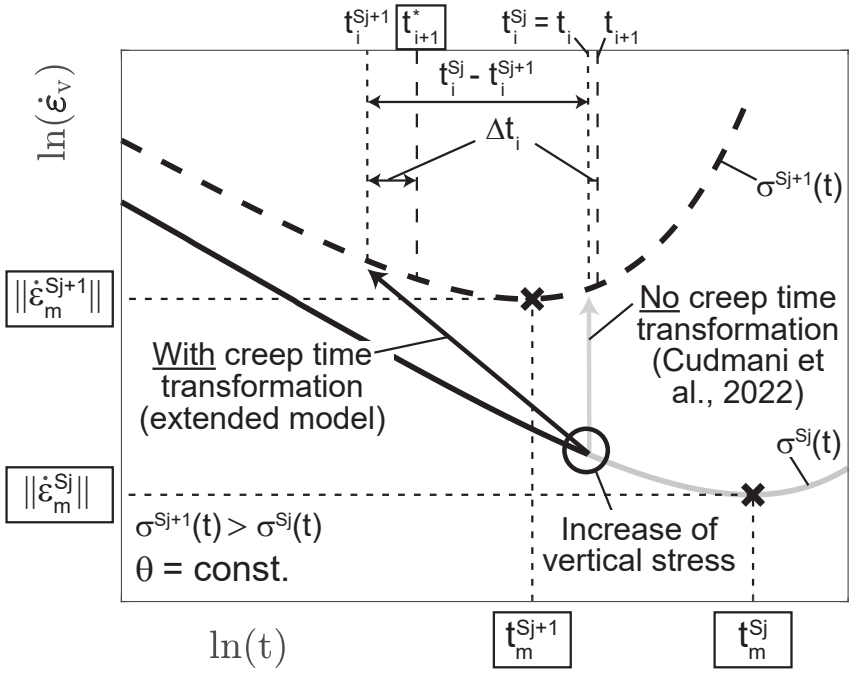

Figure 7: Generalization of the transformed creep time t^*_{i+1} for multi-stage loading

We assume that the constitutive equations 10 to 15 have been integrated from t_0 to t_i. The stress state $\boldsymbol{\sigma}^{Sj}(t)$, the viscous strain $\boldsymbol{\epsilon}_i$, and all state variables depending on stress state, temperature θ, and time t are known at the specific time t_i^{Sj}. Since we consider loading under a constant temperature θ, the time-dependent evolution of the viscous strain rate $\dot{\boldsymbol{\epsilon}}_{v,i}(t)$ (solid line in Figure 7), corresponding to single-stage creep, is defined by the stress state $\boldsymbol{\sigma}^{Sj}(t)$ according to Equations 11 to 15. In particular, the minimum strain rate $||\dot{\boldsymbol{\epsilon}}_m^{Sj}||$ and lifetime t_m^{Sj} for single-stage creep with $\boldsymbol{\sigma}^{Sj}(t)$ can be determined with Equations 12 to 15. For increment i+1, the stress increases from $\boldsymbol{\sigma}^{Sj}(t)$ to $\boldsymbol{\sigma}^{Sj+1}(t)$ and the creep time steps forward from t_i to $t_{i+1} = t_i + \Delta t_i$. For single-stage creep with $\boldsymbol{\sigma}^{Sj+1}(t)$, the viscous strain rate $\dot{\boldsymbol{\epsilon}}_{v,i+1}(t)$ (dashed line in Figure 7), the minimum strain rate $||\dot{\boldsymbol{\epsilon}}_m^{Sj+1}||$, and the lifetime t_m^{Sj+1} can be determined with Equations 11 to 15. Here, the constitutive model by Cudmani et al. (2022), which does not consider the influence of the loading history on the viscous behavior, predicts a tertiary creep strain rate with $t_{i+1} > t_m^{Sj+1}$ for this loading history in Figure 7. However, this deviates from the strain

rate evolution experimentally observed in Section 2.2, where no tertiary creep behavior after the load increase was observed, and thus $t_{i+1,exp} < t_{m,exp}$. In fact, the actual viscous strain rate $\dot{\boldsymbol{\epsilon}}_{v,i+1}\left(t^*_{i+1}\right)$ results from the single-stage creep curve for $\boldsymbol{\sigma}^{Sj+1}(t)$ by using a transformed creep time t^* instead of the global time t. In accordance with the description of the viscous strain rate under 1D conditions in Section 3, we consider the influence of the loading history on the creep behavior by including the transformed creep time t^*_{i+1} in Equation 11:

$$\dot{\boldsymbol{\epsilon}}_{v,i+1} = ||\dot{\boldsymbol{\epsilon}}_m|| \exp(-\beta) \exp\left(\beta \frac{t^*_{i+1}}{t^*_{m,i+1}}\right) \left(\frac{t^*_{i+1}}{t^*_{m,i+1}}\right)^{-\beta} \frac{\mathbf{s}}{||\mathbf{s}||} \tag{16}$$

$$t^*_{i+1} = t_{i+1} - \left(t_i^{Sj} - t_{i+1}^{Sj+1}\right) = t_i^{Sj} + \Delta t_i - \left(t_i^{Sj} - t_i^{Sj+1}\right) = t_i^{Sj+1} + \Delta t_i \tag{17}$$

$$t^*_{m,i+1} = t_m^{Sj+1} \tag{18}$$

Here, t_m^{Sj+1} is the lifetime during single-stage creep with $\sigma^{Sj+1}(t)$. In addition, t_i^{Sj+1} is the creep time required to achieve the norm of the current viscous strain $||\boldsymbol{\epsilon}_v(t_i)||$ in a single-stage creep test with $\boldsymbol{\sigma}^{Sj+1}(t_i)$. The time t_i^{Sj+1} can be determined from the solution of the following equation:

$$||\boldsymbol{\epsilon}_v(t_i)|| = ||\dot{\boldsymbol{\epsilon}}_m^{Sj+1}|| \exp(-\beta) \int_{t_0}^{t_i^{Sj+1}} \exp\left(\beta \frac{t}{t^*_{m,i+1}}\right) \left(\frac{t}{t^*_{m,i+1}}\right)^{-\beta} dt \tag{19}$$

In Equation 19, $||\boldsymbol{\epsilon}_v(t_i)||$ is the norm of the viscous strain tensor at the end of the increment i. $||\dot{\boldsymbol{\epsilon}}_m^{Sj+1}||$ and $t^*_{m,i+1}$ can be determined from Equations 12 to 15 for $\boldsymbol{\sigma}^{Sj+1}(t)$.

To sum up, the extended constitutive model able to consider multi-stage creep is defined by Equations 10 and 12 to 19. As suggested by Gudehus et al. (2008), we implemented these constitutive equations in the form of a 'user-defined material' (UMAT) FORTRAN subroutine. In this manner, the model can be used in commercial Finite Element Analysis (FEA) codes and thus is applicable in geotechnical boundary value problems. Figure 8 presents the numerical integration scheme of the extended constitutive equations for FEA.

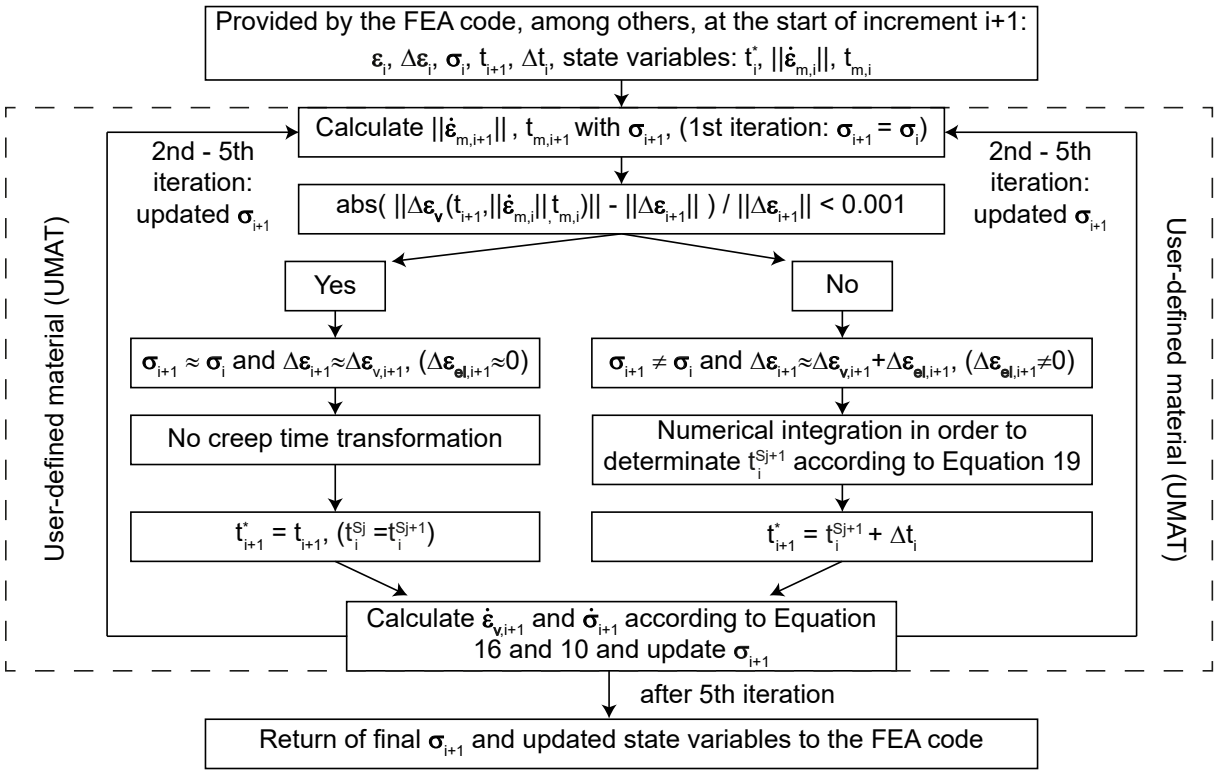

Figure 8: Numerical integration scheme of the constitutive equations for FEA to consider multi-stage creep

For the calculation of the increment i+1, the FEA code provides, among others, the stress tensor $\boldsymbol{\sigma}_i$, the total strain tensor $\boldsymbol{\epsilon}_i$, the time t_i, and the increments of the total strain tensor $\Delta\boldsymbol{\epsilon}_i$ and the time increment Δt_i, respectively. In addition, the creep time t_i^*, the minimum strain rate $||\dot{\boldsymbol{\epsilon}}_{m,i}||$, and lifetime $t_{m,i}$ of the increment i are also available as state variables. Using the incremental values provided by the FEA code, the total strain tensor $\boldsymbol{\epsilon}_{i+1} = \boldsymbol{\epsilon}_i + \Delta\boldsymbol{\epsilon}_i$ and the time $t_{i+1} = t_i + \Delta t_i$ can be determined, while the stress tensor $\boldsymbol{\sigma}_{i+1}$ has to be updated from the integration of the constitutive model. As can be seen in Figure 8, the UMAT calculation of increment i+1 consists of five iterations. For the first iteration, the minimum strain rate $||\dot{\boldsymbol{\epsilon}}_{m,i+1}||$ and the lifetime $t_{m,i+1}$ of the increment i+1 are calculated with $\boldsymbol{\sigma}_{i+1} = \boldsymbol{\sigma}_i$, because the stress tensor $\boldsymbol{\sigma}_{i+1}$ has not been updated yet. Subsequently, the norm of the total strain tensor increments $||\Delta\boldsymbol{\epsilon}_{i+1}||$ provided by the FEA code is compared with the calculated norm of the viscous strain tensor increments $||\Delta\boldsymbol{\epsilon}_{v,i+1}(t_{i+1}, ||\dot{\boldsymbol{\epsilon}}_{m,i}||, t_{m,i})||$ to identify a stress change for increment i+1. The stress $\boldsymbol{\sigma}_{i+1}$ is equal to $\boldsymbol{\sigma}_i$, if $\Delta\boldsymbol{\epsilon}_{i+1}$ only consists of a viscous strain rate component ($\Delta\boldsymbol{\epsilon}_{el,i+1} = 0$) and has approximately the same value as $\Delta\boldsymbol{\epsilon}_{v,i+1}(t_{i+1}, ||\dot{\boldsymbol{\epsilon}}_{m,i}||, t_{m,i})$. Hence, there would be no stress change between increment i and i+1, and no creep time transformation would be necessary. This strain increments (strain rate) comparison intends to avoid unnecessary computing time caused by the numerical integration to find t_i^{Sj+1} for increments without stress changes.

As can be seen in Figure 8, on the one hand, no stress changes between increments i and i+1 result in the creep time $t_{i+1}^* = t_{i+1}$. On the other hand, numerical integration is required to determine t_i^{Sj+1} according to Equation 19 when $\boldsymbol{\sigma}_{i+1}$ is not equal to $\boldsymbol{\sigma}_i$. The numerical integration in Equation 19 is solved by Newton's method to approximate t_i^{Sj+1}.

Subsequently, the transformed creep time t^{*}_{i+1} is the sum of t_i^{Sj+1} and the time increment Δt_i. After completing the first iteration process inside the UMAT subroutine, the viscous strain rate tensor $\dot{\boldsymbol{\epsilon}}_{v,i+1}$ and the resulting stress rate tensor $\dot{\boldsymbol{\sigma}}_{i+1}$ are calculated according to Equations 16 and 10. Subsequently, the stress tensor $\boldsymbol{\sigma}_{i+1} = \boldsymbol{\sigma}_{i+1} + \dot{\boldsymbol{\sigma}}_{i+1} \cdot \Delta t_i$ is updated and used for the second iteration inside the UMAT to determine $||\dot{\boldsymbol{\epsilon}}_{m,i+1}||$ and $t_{m,i+1}$ again. At the end of the iteration process (here: five iterations), the final stress tensor $\boldsymbol{\sigma}_{i+1}$ and the updated state variables are returned to the FEA code for convergence consideration.

Summarizing, the extended constitutive model presents a simple approach without introducing more material constants to consider the influence of the loading history on the creep behavior of frozen soils during steady-state temperature conditions.

5 Model validation

This section compares the prediction of the extended constitutive model with experimental data. First, we focus on the shear and creep behavior under single-stage loading. Here, it is important to verify that the novel transformed creep time t^* in Equation 16 does not influence the already validated predictive capacity of the model by Cudmani et al. (2022). Subsequently, we analyze the model response for multi-stage loading by comparing experimental and numerical results using our own test data as well as data from the literature.

5.1 Monotonic loading

Gudehus and Tamborek (1996) tested a frozen Karlsruhe sand (medium sand). The dry density $\rho_d = 1.72$ g/cm^3, void ratio e = 0.54, and the water content w = 0.18 of the frozen soil samples, were similar to the freezing test characteristics in Orth (1986). Therefore, our study adopts the material parameters for frozen Karlsruhe sand determined in (Cudmani et al., 2022), as listed in Table 3. It is worth mentioning that Cudmani et al. (2022) presented their study using the geotechnical sign convention, i.e., compressive stress is positive and tensile stress negative. In this paper, the mechanical sign convention is used (see also Section 4.1). Therefore, the 3D material parameters A, B, C, and D in Table 3 were converted accordingly to fulfill the mechanical sign convention.

Table 3: Material constants for frozen Karlsruhe sand after (Cudmani et al., 2022)

one-dimensional model							three-dimensional model *			
E	ν	c	α_1	α_2	β	K_1	A	B	C	D
[MPa]	[-]	[%]	[MPa/°C]	[-]	[-]	[K]	[-]	[-]	[-]	[-]
500	0.3	2.40	3.05	0.59	0.69	3817	2.11	-3.18	3.18	3.33
* converted to the mechanical sign convention										

Gudehus and Tamborek (1996) conducted confined compression and creep tests at a temperature of $\theta = -20$ °C under different constant traces of stress $I_\sigma = \sigma_1 + \sigma_2 + \sigma_3$. Figure 9 compares the experimental and numerical results.

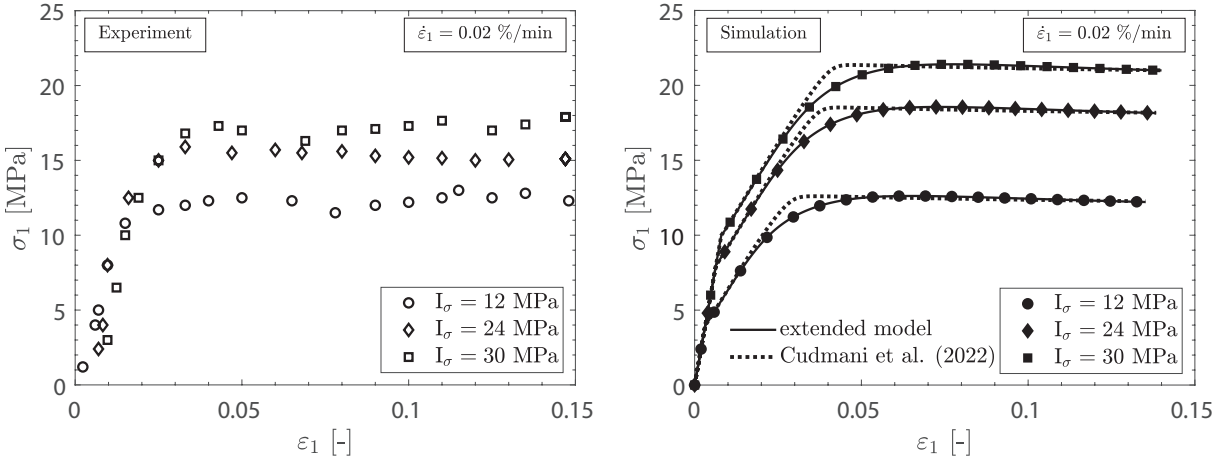

(a) Confined compression test with different constant traces of stress $I_\sigma = \sigma_1 + \sigma_2 + \sigma_3$

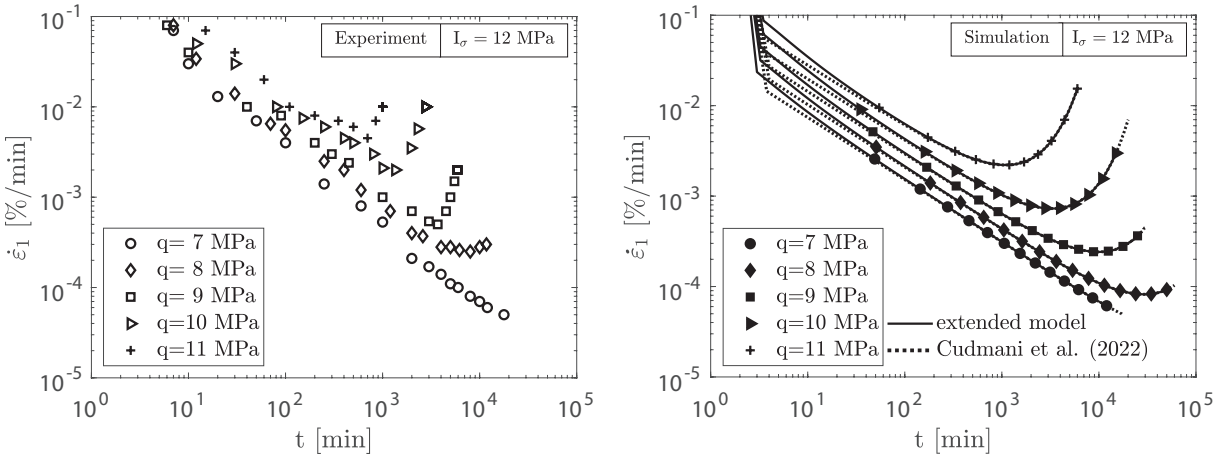

(b) Confined creep test with different deviator stresses q

Figure 9: Experimental (symbols) and numerical (solid lines with filled symbols) results of confined freezing tests at $\theta = -20$ °C [Data from (Gudehus and Tamborek, 1996)]

As can be seen, the proposed model continues to realistically predict the increasing shear resistance for increasing I_σ in confined compression tests under a constant strain rate (Figure 9a). Nevertheless, for very high stress states ($I_\sigma = 24$ MPa and $I_\sigma = 30$ MPa), the measured compressive peak strength does not increase significantly. Gudehus and Tamborek (1996) explained this finding as being due to the pressure-dependent reduction of the freezing point. As a result, this reduction led to ice softening and, simultaneously, a reduction of the shear resistance between the ice matrix and the grain skeleton. These weakening effects are complex and difficult to calculate numerically. Therefore, the simulation of the confined compression tests in Figure 9a leads to a slight overestimation of the peak strength for very high stress states.

In addition, slight differences can be observed between the simulations with the model by Cudmani et al. (2022) (dashed lines) and the extended model presented in this study (solid lines) for the confined compression tests in Figure 9a (right side). The use of the extended model improves the description of the actual deformation behavior as the ultimate shear strength $q_u = \sigma_1 - \sigma_3$ reaches the peak shear deformation $\epsilon_{u,1} > 0.06$ more slowly. In contrast, the predicted behavior with the model by Cudmani et al. (2022) is stiffer ($\epsilon_{u,1} > 0.06$) than observed in the experiments. Hence, the model accuracy improves in

terms of the shear behavior of frozen soil through the proposed equivalent creep time.
In addition, the comparison of confined creep tests with $I_\sigma = 12$ MPa and different deviator stresses q at $\theta = -20$ °C is depicted in Figure 9b. The evolution of the axial strain rate over time is slightly underestimated by the extended model. In fact, the simulated minimum axial strain rates $\dot{\epsilon}_m$ are lower in comparison to the experiments. As a result, the predicted lifetime t_m becomes longer. As expected, there are no essential differences between the model response by Cudmani et al. (2022) (dashed lines) and the extended model (solid lines). The introduction of the transformed creep time t^* in Equation 16 does not change the model response in terms of the predicted creep behavior.
In summary, the implementation of the transformed creep time t^* improves the model response for monotonic shearing without having any noteworthy influence on the model accuracy for single-stage loaded creep.

5.2 Multi-stage loaded creep

5.2.1 Using our own test data

After confirming the model response for single-stage loading, we investigate the validation for multi-stage loading by simulating the multi-stage creep tests described in Section 2.2. According to Cudmani et al. (2022), seven material constants have to be determined for the 1D model. The material parameters determined in (Cudmani et al., 2022) based on Orth's (1986) experimental findings cannot be used for our analysis. Our own freezing test characteristics are different from those in (Orth, 1986) mainly due to the different dry density of our tested frozen sand samples (for influences on testing results, see, e.g., (Ting et al., 1983)). Therefore, it is necessary to re-calibrate the model parameters using our own testing data. According to Cudmani et al. (2022), at least two uniaxial creep tests and three uniaxial compression tests are needed to determine the seven 1D-material constants. Thus, we performed additional uniaxial creep and compression tests to avoid using the same experimental data for the model calibration and validation. The most important results of these additional tests are summarized in Table 4.

Table 4: Additional testing data to calibrate the 1D-model

Uniaxial creep tests with constant loads				
Test number	θ [°C]	σ_1 [MPa]	$\dot{\epsilon}_m$ [%/min]	t_m [min]
M-7	-10.0	6.5	6.50 E-3	334.2
M-8	-10.0	8.8	9.01 E-2	25.8

Uniaxial compression tests			
Test number	θ [°C]	σ_c [MPa]	$\dot{\epsilon}_1$ [%/min]
C-1	-10.0	10.4	1.0
C-2	-15.0	13.7	1.0
C-3	-20.0	16.5	1.0

The method to determine the 1D-material constants using experimental data is extensively described in (Cudmani et al., 2022) and (Orth, 1986) and will not be repeated

here. The material parameters used for the 1D-model are presented in Table 5.

Table 5: Material constants for the 1D model

E	ν	c	α_1	α_2	β	K_1
[MPa]	[-]	[%]	[MPa/°C]	[-]	[-]	[K]
500	0.3	2.40	2.44	0.63	0.69	3817

The results of the uniaxial experimental and numerical multi-stage creep tests are compared in Figure 10. Note that the experimental test results of MT1 to MT3 have already been introduced in Section 2, viz. Table 2 and Figure 3.

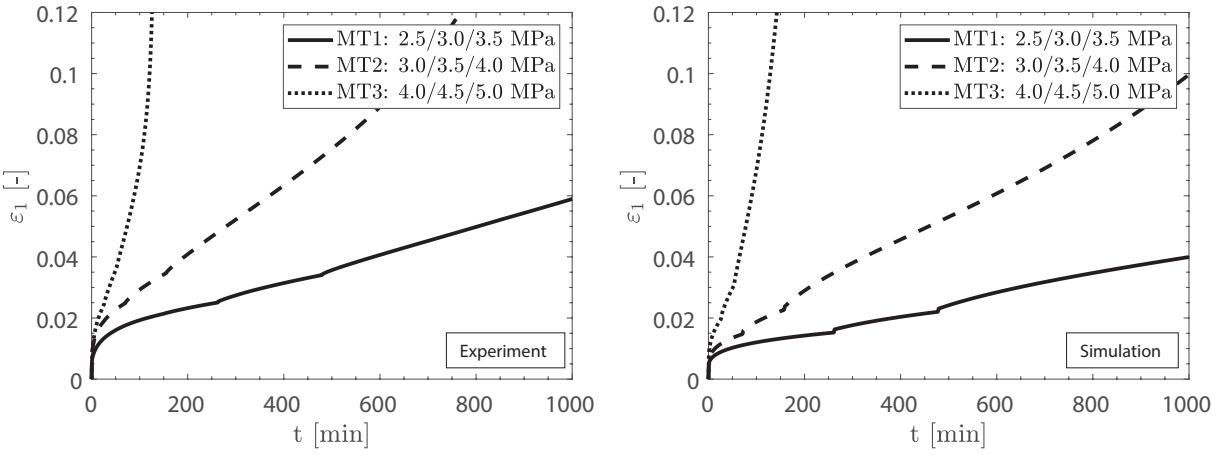

(a) Axial strain evolution over time

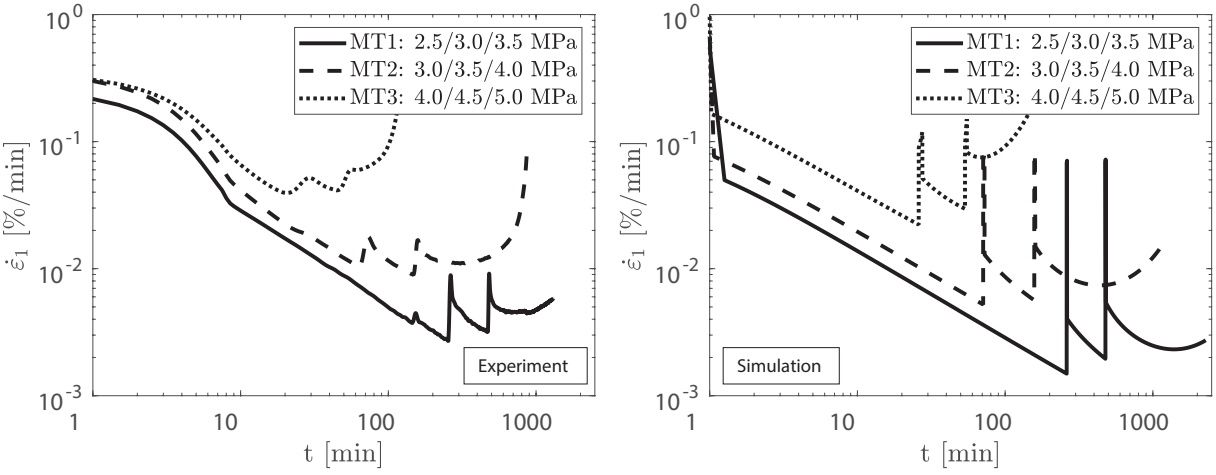

(b) Axial strain rate evolution over time

Figure 10: Experimental and numerical results of uniaxial multi-stage creep tests at $\theta = -4.3$ °C

The model prediction agrees well with the experimental data. The minimum axial strain rate $\dot{\epsilon}_{m,1}$ and the lifetime t_m for the last load step are in accordance, thus confirming that the proposed constitutive model extension is appropriate.

To extend the model validation, we simulated uniaxial multi-stage creep tests at different temperatures using data from the literature. This discussion follows in the next section.

5.2.2 Using data from the literature

As mentioned in the introduction, Eckardt (1979a,b, 1982) extensively investigated the mechanical behavior of frozen sand with the help of single-stage and multi-stage creep tests under compressive stress states. The granulometric properties (grain size distribution) and state variables (void ratio, degree of saturation, water content, and dry density) of Eckardts tested frozen medium sand were very similar to the freezing tests by Orth (1986), who investigated frozen Karlsruhe sand in the same frost laboratory at the University of Karlsruhe (Germany). Thus, we also adopted the determined material parameters for frozen Karlsruhe sand in Table 3 for the tested sand by Eckardt. The experimental and numerical results of uniaxial multi-stage creep tests for different increasing vertical stresses at $\theta = -10$ °C and $\theta = -20$ °C are shown in Figure 11.

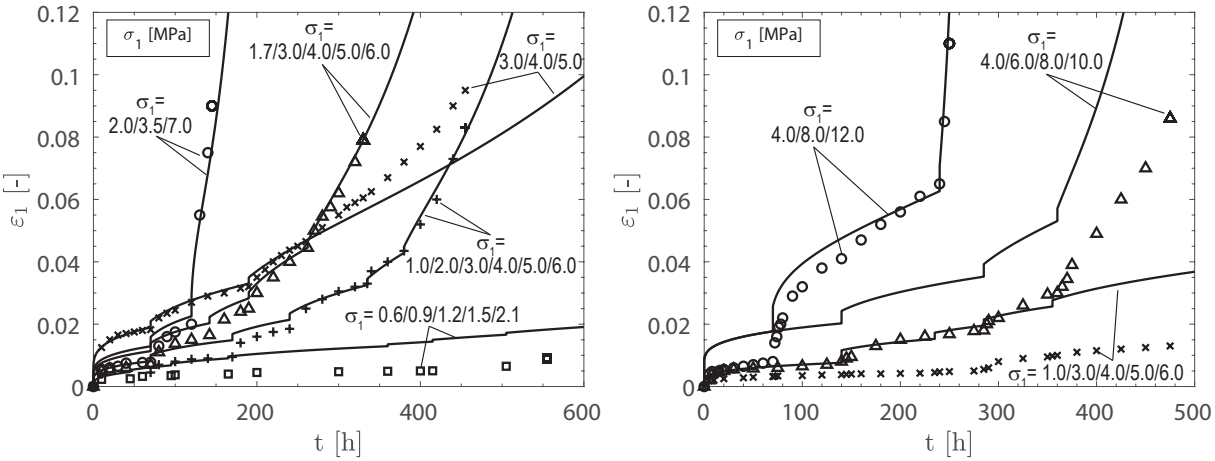

(a) $\theta = -10$ °C [Data from (Eckardt, 1979b)] (b) $\theta = -20$ °C [Data from (Eckardt, 1982)]]

Figure 11: Evolution of axial strain over time: Experimental (symbols) and numerical (solid lines) results of uniaxial multi-stage creep tests

The multi-stage creep tests include three to six load steps $N^{\sigma_1,j}$ ($j = 3 - 6$) with incremental stress increases $\Delta\sigma_1$ between 0.3 to 4.0 MPa. The vertical stress σ_1 for each load step ranged from 0.6 to 12.0 MPa.

The model accuracy concurs more strongly at $\theta = -10$ °C (Figure 11a) when compared to $\theta = -20$ °C (Figure 11b). The deviations between the calculated and measured deformations at $\theta = -20$ °C occur during the load applications due to stiffness differences. Here, the simulations overestimate the actual elastic deformations during the load application in comparison with the deformations observed in the experiments. However, the creep deformations (evolution of the predominantly viscous axial strain) for every loading step are in good accordance.

For both the experiments and the simulations, the time-dependent axial strain increases

as a function of the stress state. As shown in Figure 4, the average axial strain ϵ_{m} at the turning point ($\mathrm{t} = \mathrm{t}_{\mathrm{m}}$) for this frozen Karlsruhe sand is around 0.04 to 0.06. The model realistically captures the turning point of the creep curves in accordance with the experiments in Figure 11, as the axial strains increase strongly for $\epsilon_1 > 0.06$ and creep failure occurs.

In fact, there are two simulations in Figure 11, one at $\theta = -10$ °C with $\sigma_1 = 2.0/3.5/7.0$ MPa and one at $\theta = -20$ °C with $\sigma_1 = 4.0/8.0/12.0$ MPa, which both predict creep failure immediately after the last load increase. The model response concurs with the corresponding experiments that also show creep failure shortly after the last load step. The proposed models ability to predict creep failure after a load increase is a powerful feature for safely improving the geotechnical design of frozen soil bodies. The consideration of multi-stage creep provides clear economic benefits as the lifetime of the frozen soil is ultimately longer in comparison to a single-stage lifetime evaluation under the same loading stages. In addition, our proposed model extension guarantees the early identification of sudden creep failure. Besides, for very long creep times (here: $\mathrm{t} > 500$ h) under low stress states ($\sigma_1 = 0.6/0.9/1.2/1.5/2.1$ MPa and $\sigma_1 = 1.0/3.0/4.0/5.0/6.0$ MPa) the model does not predict creep failure which is also in accordance with the corresponding experiments. Therefore, we assume that the over-engineering of frozen soil bodies by using the model is unlikely.

Summarizing, the essential features of the rate-, stress-, and temperature-dependent characteristics of frozen soils are well reproduced by the model for multi-stage loaded creep. Moreover, the improved model can precisely predict the rate-dependent evolution of axial strain, both for different numbers of load steps $\mathrm{N}^{\sigma_1,\mathrm{j}}$ and for varying stress with increasing $\Delta\sigma_1$. Here, the model validation includes a very large stress state range σ_1.

6 Limitations and recommendations for the use of the constitutive model

Cudmani et al. (2022) have already discussed several shortcomings of the constitutive model, e.g., upper and lower strain rate boundaries and predominantly monotonic loading. Even though the improved, far-reaching constitutive model tackles some of these issues, we should point out that some limitations remain.

Mechanical behaviour upon unloading

Despite the efforts made so far (e.g., (Andersland and Akili, 1967; Zhou et al., 2016; Li et al., 2017)), there is a lack of sophisticated experimental data regarding the creep behavior of frozen soils under stepwise unloading or a combination of loading and unloading. We plan to close this gap in experimental knowledge and confirm the presented approach accordingly. Nevertheless, from a practical point of view, the current model version is suitable for predicting the creep behavior during decreasing stress states at constant temperatures. According to studies such as (Zhou et al., 2022), we expect a similar positive influence from the overconsolidation ratio (OCR) on the creep rate of frozen soils upon unloading, as with unfrozen soils (Levin et al., 2019). If we disregard these concerns, the current model response is on the safe side for unloading creep stages in steady-state temperature conditions.

Strain rate changes during shearing

Orth (1986) performed uniaxial compression tests of frozen sand with varying strain rates $\dot{\epsilon}_1$ at a constant temperature. The uniaxial compressive strength σ_c for stepwise increasing or decreasing strain rates was not similar to that under a constant strain rate. Orth (1986) argued that changing strain rates strongly influence the initiation and propagation of cracks in the ice matrix. Hence, uniaxial compression tests with varying strain rates were not directly comparable to tests with a constant strain rate due to different viscous behaviors. In contrast, based on confined compression tests with frozen clay under constant and varying strain rates at a constant temperature, Wang et al. (2017) suggested a potentially unique stress-strain relationship for a given strain rate. This would be consistent with the isotach theory proposed for unfrozen clays (Šuklje, 1957). Despite these efforts, the influence of varying strain rates on the mechanical behavior of frozen soils has not been fully understood. Our currently proposed model does not consider a possible influence of varying strain rates on the shear behavior of frozen soils. The predicted stress state is uniquely defined by the current strain and strain rate under a constant temperature.

Influence of varying temperatures

The mechanical behavior of frozen soils changes not only in cases of varying stress states under constant temperatures but also for varying temperatures at constant stress states. However, there are few experimental studies like (Wang et al., 2017; Yao et al., 2018; Wang et al., 2022) dealing with the influence of transient temperature conditions on the shear and creep behavior of frozen soils. According to Andersland and Ladanyi (2003), decreasing temperatures can result in (partial) refreezing of the developed cracks in the frozen soil. As a result, the creep rates sharply decrease. In contrast, increasing temperatures lead to ice softening, a possible increase in the unfrozen water content, and an overall reduction of shear and creep strength (Wang et al., 2022). The proposed concept may be further adjusted to consider these highly non-linear characteristics. At this

stage, we suggest limiting the use of the constitutive model for steady-state temperature conditions.

7 Conclusion

This study deals with the influence of varying stress states on the mechanical behavior of frozen soils at constant temperatures. The comparison between unaxial creep tests with both single-stage loading and multi-stage loading shows that the minimum axial strain rate $\dot{\epsilon}_\mathrm{m}$ is mostly independent of the loading history. In contrast, the lifetime $\mathrm{t_m}$ of the frozen soil depends on the loading history. These findings are consistent with previous experimental studies found in the literature.
Moreover, the introduction of the transformed creep time t^* enables the conversion of multi-stage creep tests into equivalent single-stage creep tests. Here, the evolution of the normalized axial strain rate $\dot{\epsilon}_1/\dot{\epsilon}_\mathrm{m}$ over normalized time $\mathrm{t}/\mathrm{t_m}$ for single-stage as well as the normalized axial strain rate $\dot{\epsilon}_1/\dot{\epsilon}_\mathrm{m}$ over normalized transformed time $\mathrm{t}^{*,\mathrm{Mj}}/\mathrm{t}_\mathrm{m}^{*,\mathrm{Mj}}$ for multi-stage creep tests converge and are consequently comparable with each other. Hence, this crucial relationship of the constitutive model for frozen soils proposed by Cudmani et al. (2022) to describe the rate-, stress-, and temperature-dependent mechanical behavior of frozen soils is not only valid for predominantly monotonic (single-stage) loading but also for multi-stage loading. Therefore, we extend the constitutive model by taking into account multi-stage loading based on our proposed determination of the normalized axial strain rate $\dot{\epsilon}_1/\dot{\epsilon}_\mathrm{m}$ over normalized transformed time $\mathrm{t}^{*,\mathrm{Mj}}/\mathrm{t}_\mathrm{m}^{*,\mathrm{Mj}}$.
The extended model captures the equivalent creep time after a changing stress state by coupling the transformed creep time t^* to the previous loading history. Comparing the simulations with our own experiments and comprehensive data from the literature successfully completes the first step in validating the extended model. The model validation includes a large number of incremental axial stress changes $\mathrm{N}_{\sigma_1,\mathrm{step}}$, and incremental axial stress increases $\Delta\sigma_1$ by simultaneously covering a wide range of total axial stress states σ_1. Considering the influence of varying stress states on the shear and creep behavior of frozen soils enables a more realistic and economically optimized design of ground freezing applications due to the resulting prolonged lifetime of the frozen soil. In fact, it is possible to take into account different construction stages and techniques and, therefore, different stress levels of the frozen soil body.
In summary, this study has significantly improved and further validated an existing numerical tool for assessing the stability and deformations of frozen soils in engineering applications for single-stage and multi-stage loading.

Competing interests

The authors declare there are no competing interests.

Data availability

Some or all data, models, or code that support the findings of this study are available from the corresponding author upon reasonable request.

Funding statement

The authors declare no specific funding for this work.

Notation

$\boldsymbol{\epsilon}$ total strain tensor
$\boldsymbol{\epsilon}_{\mathrm{el}}$ elastic strain tensor
$\boldsymbol{\epsilon}_{\mathrm{v}}$ viscous strain tensor
$\dot{\boldsymbol{\epsilon}}$ total strain rate tensor
$\dot{\boldsymbol{\epsilon}}_{\mathrm{el}}$ elastic strain rate tensor
$\dot{\boldsymbol{\epsilon}}_{\mathrm{v}}$ viscous strain rate tensor
ϵ_1 axial strain
$\dot{\epsilon}_1$ axial strain rate
ϵ_{m} average axial strain at the lifetime of the frozen soil
$\dot{\epsilon}_{\alpha}$ reference strain rate
$\dot{\epsilon}_{\mathrm{m}}$ minimum creep rate / minimum axial strain rate
$\dot{\boldsymbol{\epsilon}}_{\mathrm{m}}$ minimum creep rate tensor
t_{m} lifetime of the frozen soil after which tertiary creep starts
Θ temperature in Celsius
t actual testing time / global total time
t_0 starting creep time
t^* transformed creep time
p Roscoe's invariant representing mean pressure
q Roscoe's invariant representing deviator pressure
σ_1 axial stress
σ_{cr} equivalent uniaxial creep strength
$\boldsymbol{\sigma}$ stress tensor
$\dot{\boldsymbol{\sigma}}$ stress rate tensor
$\mathbf{s}$ deviatoric part of stress tensor
$\mathrm{I}_{\boldsymbol{\sigma}}$ trace of stress
$\mathbf{L}$ fourth-order isotropic elastic stiffness tensor
E Young's modulus
ν Poisson's ratio
ϕ Lode angle
ρ_{d} dry density of the frozen soil sample
w gravimetric water content
S_{r} degree of saturation
e void ratio

References

Andersland, O. B. and Akili, W. (1967). Stress Effect on Creep Rates of a Frozen Clay Soil. *Géotechnique*, 17(1):27–39. doi:10.1680/geot.1967.17.1.27.

Andersland, O. B. and Ladanyi, B. (2003). *Frozen ground engineering*. Wiley, New York and Chichester, 2nd ed. edition.

Classen, J., Hoppe, P., and Seegers, J. (2019). Ground freezing and excavation of the museum island metro station under a river in central berlin–challenges and experiences. In *Tunnels and Underground Cities: Engineering and Innovation meet Archaeology, Architecture and Art*, pages 1314–1322. CRC Press.

Cudmani, R. and Nagelsdiek, S. (2006). FE-Analysis of ground freezing for the construction of a tunnel cross connection. In Triantafyllidis, T., editor, *Proceedings of the international conference on numerical modelling of construction processes in geotechnical engineering for urban environment*, pages 201–11, Boca Raton, FL, USA: CRC Press.

Cudmani, R., Yan, W., and Schindler, U. (2022). A constitutive model for the simulation of temperature-, stress- and rate-dependent behaviour of frozen granular soils. *Géotechnique*, 0(0):1–36. doi:10.1680/jgeot.21.00012. Ahead of Print.

Eckardt, H. (1979a). Creep behaviour of frozen soils in uniaxial compression tests. *Engineering Geology*, 13(1):185–195. doi:10.1016/0013–7952(79)90031–0.

Eckardt, H. (1979b). *Tragverhalten gefrorener Erdkörper*. PhD thesis, Institut für Bodenmechanik und Felsmechanik der Universität Fridericiana in Karlsruhe. Vol. 81. (in German).

Eckardt, H. (1982). Creep tests with frozen soils under uniaxial tension and uniaxial compression. In *Proceedings of the 4th Canadian Permafrost Conference*, pages 365–373, Calgary, Canada.

Enokido, M. and Kameta, J. (1987). Influence of water content on compressive strength of frozen sands. *Soils and Foundations*, 27(4):148–152. doi:10.3208/sandf1972.27.4_148.

Ghoreishian Amiri, S., Grimstad, G., Kadivar, M., and Nordal, S. (2016). Constitutive model for rate-independent behavior of saturated frozen soils. *Canadian Geotechnical Journal*, 53(10):1646–1657. doi:10.1139/cgj–2015–0467.

Gudehus, G., Amorosi, A., Gens, A., Herle, I., Kolymbas, D., Mašín, D., Muir Wood, D., Niemunis, A., Nova, R., Pastor, M., et al. (2008). The soilmodels. info project. *International Journal for Numerical and Analytical Methods in Geomechanics*, 32(12):1571–1572. doi:10.1002/nag.675.

Gudehus, G. and Tamborek, A. (1996). Zur Kraftübertragung Frostkörper - Stützelemente. *Bautechnik*, 73(9):570–81. (in German).

Han, L., Ye, G.-l., Li, Y.-h., Xia, X.-h., and Wang, J.-h. (2016). In situ monitoring of frost heave pressure during cross passage construction using ground-freezing method. *Canadian Geotechnical Journal*, 53(3):530–539. doi:10.1139/cgj–2014–0486.

Harris, J. S. (1995). *Ground freezing in practice*. Thomas Telford Services Ltd, London, UK.

Lade, P. V. (2016). *Triaxial testing of soils*. John Wiley & Sons Inc, Hoboken. doi:10.1002/9781119106616.

Levin, F., Vogt, S., and Cudmani, R. (2019). Time-dependent behaviour of sand with different fine contents under oedometric loading. *Canadian Geotechnical Journal*, 56(1):102–115. doi:10.1139/cgj–2017–0565.

Li, D., Yang, X., and Chen, J. (2017). A study of triaxial creep test and yield criterion of artificial frozen soil under unloading stress paths. *Cold Regions Science and Technology*, 141:163–170. doi:10.1016/j.coldregions.2017.06.009.

Nishimura, S. and Wang, J. (2019). A simple framework for describing strength of saturated frozen soils as multi-phase coupled system. *Géotechnique*, 69(8):659–671. doi:10.1680/jgeot.17.P.104.

Orth, W. (1986). *Gefrorener Sand als Werkstoff: Elementversuche und Materialmodell*. PhD thesis, Institut für Bodenmechanik und Felsmechanik der Universität Fridericiana in Karlsruhe. Vol. 100. (in German).

Orth, W. (2018). Bodenvereisung. *Grundbau-Taschenbuch, Teil 2: Geotechnische Verfahren*, pages 299–373. Wilhelm Ernst & Sohn, Berlin, Germany. (in German).

Phillips, M., Fadhel, H., Raafat, I., and El-Kelesh, A. (2021). Use of artificial ground freezing in construction of cross passages under Suez Canal. *Geomechanics and Tunnelling*, 14(3):298–307. doi:10.1002/geot.202000045.

Pimentel, E. and Anagnostou, G. (2019). Design of artificial ground freezing for an access tunnel of a railway station in Switzerland. In *Tunnels and Underground Cities: Engineering and Innovation meet Archaeology, Architecture and Art*, pages 1479–1488. CRC Press.

Russo, G., Corbo, A., Cavuoto, F., and Autuori, S. (2015). Artificial Ground Freezing to excavate a tunnel in sandy soil. Measurements and back analysis. *Tunnelling and Underground Space Technology*, 50:226–238. doi:10.1016/j.tust.2015.07.008.

Šuklje, L. (1957). The analysis of the consolidation process by the isotache method. In *Proceedings of the 4th international conference on soil mechanics and foundation engineering*, volume 1, pages 200–206, London, UK.

Ting, J. M., Martin, R. T., and Ladd, C. C. (1983). Mechanisms of strength for frozen sand. *Journal of Geotechnical Engineering*, 109(10):1286–1302. doi:10.1061/(ASCE)0733–9410(1983)109:10(1286).

Vyalov, S. S., Slepak, M. E., Maksimyak, R. V., and Chapayev, A. A. (1989). Frozen soil deformations and failure under different loading. In *Proceedings of the Fifth International Symposium on Ground Freezing*, pages 465–471, Rotterdam, Netherlands.

Wang, J., Nishimura, S., and Tokoro, T. (2017). Laboratory study and interpretation of mechanical behavior of frozen clay through state concept. *Soils and Foundations*, 57(2):194–210. doi:10.1016/j.sandf.2017.03.003.

Wang, P., Liu, E., Zhi, B., Song, B., and Kang, J. (2022). Creep characteristics and unified macro–meso creep model for saturated frozen soil under constant/variable temperature conditions. *Acta Geotechnica*, 17:5299–5319. doi:10.1007/s11440–022–01586–6.

Xu, G., Peng, C., Wu, W., and Qi, J. (2017). Combined constitutive model for creep and steady flow rate of frozen soil in an unconfined condition. *Canadian Geotechnical Journal*, 54(7):907–914. doi:10.1139/cgj–2016–0139.

Yao, X., Qi, J., Zhang, J., and Yu, F. (2018). A one-dimensional creep model for frozen soils taking temperature as an independent variable. *Soils and Foundations*, 58(3):627–640. doi:10.1016/j.sandf.2018.03.001.

Zhao, Y., Zhang, M., and Gao, J. (2023). Research progress of constitutive models of frozen soils: A review. *Cold Regions Science and Technology*, 206:103720. doi:10.1016/j.coldregions.2022.103720.

Zhou, Z., Bai, R., Shen, M., and Wang, Q. (2022). The effect of overconsolidation on monotonic and cyclic behaviours of frozen subgrade soil. *Transportation Geotechnics*, 32:100710. doi:10.1016/j.trgeo.2021.100710.

Zhou, Z., Ma, W., Zhang, S., Du, H., Mu, Y., and Li, G. (2016). Multiaxial creep of frozen loess. *Mechanics of Materials*, 95:172–191. doi:10.1016/j.mechmat.2015.11.020.

Zhou, Z., Ma, W., Zhang, S., Mu, Y., and Li, G. (2020). Experimental investigation of the path-dependent strength and deformation behaviours of frozen loess. *Engineering Geology*, 265:105449. doi:10.1016/j.enggeo.2019.105449.

Zhou, Z., Zhao, J., Tan, Z., and Zhou, X. (2021). Mechanical responses in the construction process of super-large cross-section tunnel: A case study of Gongbei tunnel. *Tunnelling and Underground Space Technology*, 115:104044. doi:10.1016/j.tust.2021.104044.